

WINTER SEA ICE MAPPING FROM MULTI-PARAMETER SYNTHETIC APERTURE RADAR DATA

Eric Rignot and Mark R. Drinkwater

*Jet Propulsion Laboratory, California Institute of Technology
4800 Oak Grove Drive
Pasadena, CA 91109*

Submitted to: the Journal of **Glaciology**, on March 22, 1993

ABSTRACT

Airborne polarimetric synthetic aperture radar observations of winter sea-ice collected in the Beaufort sea in March 1988 at C- ($\lambda = 5.6\text{cm}$), L- ($\lambda = 24\text{cm}$) and P- ($\lambda = 68\text{cm}$) band frequencies are used to identify 6 ice conditions: 1) multiyear sea-ice; 2) compressed first-year ice; 3) first-year rubble and ridges; 4) first-year rough ice; 5) first-year smooth ice; and 6) thin ice. Validation of these ice conditions is based on aerial photos, weather and ice surface measurements collected at an ice camp, together with airborne passive microwave imagery, radar backscatter model predictions, and visual analysis of the SAR data. Ice mapping works best using L- and C-band polarimetric combined (90% classification accuracy). C- and L-band at a single polarization yield 67% and 71% classification accuracy because C-band confuses multiyear ice and rough, compressed, thick first-year ice surrounding multiyear ice floes; and L-band confuse multiyear ice and rough, ridged first-year ice. P-band offers poor discrimination for separating all ice types. At one frequency, adding a second polarization significantly increases classification accuracy, especially at L-band (85% accuracy), and separates calm open water from thin ice. At a single polarization, combining L- and C-band yield classification accuracies equivalent to that obtained using L- and C-band polarimetric combined. The results are used to predict the limitations of currently available single-frequency single-polarization spaceborne SAR sensors for winter sea-ice mapping.

1. INTRODUCTION

Sea ice is an important modulator of regional and global climate because of the insulating layer which it forms between the cold polar air masses and the relatively warm oceans beneath the ice. To understand the feedbacks between sea-ice and climate change, extensive spaceborne observations as well as *in-situ* measurements are necessary over long periods of time (Carsey, 1989). In recent years, synthetic aperture radars (SAR) have received an increasing level of attention because of their all weather, day and night capability, their high spatial resolution from space, and their potential for sea-ice studies. SAR observations of sea-ice have been used to study the kinematics and deformation of the ice field (Fily and Rothrock, 1990), and algorithms have been developed to automatically and routinely generate ice motion maps (Kwok and others, 1990) at the Alaska SAR Facility (ASF) in Fairbanks, Alaska, using single-frequency single-polarization spaceborne SAR data from the European Remote Sensing Satellite, ERS-1 (Attema, 1991). Similarly, ice type and ice concentration maps are routinely generated at ASF using ERS-1 SAR data (Kwok and others, 1992). The ice classification software separates multiyear ice, first-year rough and smooth ice, and new ice / smooth open water (at the system noise power level) based on their radar backscatter characteristics. The spatial variability of the distribution of ice types is used as a proxy indicator of the regional variability of ice thickness, a required parameter for estimating the dynamic and thermodynamic balance of the polar regions.

Numerous theoretical studies (e.g., Tsang and Kong, 1981; Lim and others, 1984; Tsang and Ishimaru, 1987), *in-situ* ground observations (Onstott and others, 1987), and controlled experiments (Bredow and others, 1989) indicate that multichannel

SAR instruments could further improve our current capability to identify different ice conditions, and add the possibility of extracting geophysical parameters of importance such as snow cover characteristics, ice salinity, and thickness of the thin first-year ice (Winebrenner and others, 1989) directly from the microwave ice signatures. The first examples of multifrequency polarimetric SAR observations of sea-ice, acquired by the NASA/Jet Propulsion laboratory aircraft SAR (abbrev. AIRSAR) in March 1988 over the Beaufort, Chukchi, and Bering seas (Drinkwater and others, 1991) confirmed that multifrequency and polarimetric information could distinguish different sub-categories of first-year sea-ice better, and separate thin-ice from open water. In this paper, we evaluate on a quantitative basis the added value of various frequencies and polarizations for mapping ice conditions and for estimating ice fractions. Ice maps derived from multi-parameter SAR data and validated using a combination of ancillary information are used as a yardstick to predict the level of performance of current and future single-frequency single-polarization satellite SAR systems for winter ice mapping such as ER - 1 SAR, the Japanese Earth Resources Satellite J-ERS-1 SAR (Nemoto and others, 1991), and the Canadian RADARSAT SAR (Raney and others, 1991), and possible combined information from these active sensors. The 6 identified winter ice conditions are: 1) multiyear sea-ice (MY), 2) compressed first year sea-ice (CFY); 3) first-year rubble and ice ridges (FYRR); 4) first-year rough ice (FYR); 5) first-year smooth ice (FYS); and 6) thin first-year ice (ThI). Although open water is absent from all analyzed data, it is included in the discussion as a possible ice type.

2. AIRSAR DATA SET

AIRSAR acquired SAR observations of sea-ice in March 1988 over the Beaufort Sea,

North of Alaska, at C- ($\lambda = 5.6\text{cm}$), L- ($\lambda = 24\text{cm}$), and 1'- ($\lambda = 68\text{cm}$) band frequencies. At each frequency, the complete scattering matrix (van der Hulst, 1981; van Zyl and Ulaby, 1990) of each resolution element is recorded, and the data are processed such that the scattering matrices acquired at different frequencies are spatially registered. A scattering matrix comprises 4 complex numbers $S_{HH}, S_{HV}, S_{VH}, S_{VV}$, where S_{VH} is a complex number representation of the amplitude and phase of the radar return received at V- (vertical) polarization when H- (horizontal) polarization is transmitted. Subsequent SAR processing yields SAR data in Stokes format (Ulaby and Elachi, 1990), or equivalently in cross-product format, i.e. for each pixel element the cross-products $\langle S_{XY} S_{X'Y'}^* \rangle$ are stored, where X, Y, X', and Y' are H or V's, an asterisk denotes complex conjugation, and $\langle \rangle$ indicates a spatial averaging process over several (4 in practice) contiguous elements called multilook processing in the SAR literature. Although there are 16 cross-products for each pixel element, a number of them are of second order magnitude for a large variety of natural distributed targets (Borgeaud and others, 1987; Nghiem and others, 1992), leaving only 4 cross-products for complete characterization of the polarimetric characteristics of a natural target, or equivalently the following 5 real numbers

$$\begin{aligned} \sigma_{HH} &= \langle S_{HH} S_{HH}^* \rangle; \sigma_{HV} = \langle S_{HV} S_{HV}^* \rangle; \sigma_{VV} = \langle S_{VV} S_{VV}^* \rangle, \\ \rho_{HHVV}^* &= \frac{|\langle S_{HH} S_{VV}^* \rangle|}{\sqrt{\langle S_{HH} S_{HH}^* \rangle} \sqrt{\langle S_{VV} S_{VV}^* \rangle}}; \phi_{HHVV}^* = \angle(\langle S_{HH} S_{VV}^* \rangle) \end{aligned} \quad (1)$$

$\angle(x)$ denotes the phase of the complex number x . The polarimetric dimension ϕ_{HHVV}^* is present in ρ_{HHVV}^* . The radar backscatter σ 's are normalized (by the projected area of a pixel element) intensities, expressed in dB by taking ten times the base ten logarithm of their magnitude.

A total of 10 scenes from the Beaufort sea were processed at 12 m resolution in

cross-product format, but we limited the present analysis to 2 scenes, acquired at different dates and locations, that are representative of typical ice conditions in the Beaufort sea in March 1988, and for which we have sufficient ancillary information for validating the ice type labels. The 2 scenes were acquired in a transition zone between the extensive near-shore first-year ice region and the multiyear polar ice pack to the North. Image 1372 was acquired at a center location of $73^{\circ}2.9'N$, $142^{\circ}17.1'W$ at 17:19:55 GMT on March 11, 1988, and is shown in Figure 1a at C-band VV-polarization and in Figure 1b at L-band HH-polarization. Near range is on top, with the aircraft flying from right to left, looking to its left, and heading North. Pixel spacing is 6.7m in range by 12.1m in azimuth. The scene is 12 km by 8 km in size on the ground, and the incidence angle θ_i of the radar illumination onto the surface varies between 29.3° and 52.4° from top to bottom. Image 1372 is one of the few scenes acquired in the Beaufort sea in March 1988 where thin ice could be identified in a recently frozen lead. Image 311, shown in Figure 2a at C-band VV-polarization and in Figure 2b at L-band HH-polarization, was acquired at a center location of $72^{\circ}38.2'N$, $143^{\circ}48.1'W$ at 04:35:08 GMT on March 19, 1988. θ_i varies between 19.8° and 50.2° across range. The buildings of the Applied Physics Laboratory (API), drifting ice station (API, IS'88) (Wen and others, 1989) appear as a bright point target at the edge of a large bright multiyear ice floe (Fig. 2a).

An accurate radiometric and polarimetric calibration of the SAR data is not necessary for segmenting and classifying SAR data, but it is required for correct physical analysis of the extracted microwave signatures. Calibration of the phase difference ϕ_{HHVV} , and cross-talk removal between the H and V polarized radar channels (van Zyl, 1990) were performed for both scenes assuming that multiyear sea-ice is an azimuthally symmetric random medium (Nghiem and others, 1993) as the hummocky

topography of multiyear sea-ice and its air-bubbles inclusions do not show any azimuthal preference (Weeks and Ackley, 1982). The gain imbalance between the H and V polarized radar channels was determined to be accurate to within 1 dB at L- and C-band, and 2.5 dB at P-band from a study of the radar performance during that period (Freeman, 1990). In the absence of external calibration devices deployed in the scene prior to flight, we adjusted the absolute gain of the radar manually to reproduce published scatterometer measurements of multiyear ice under cold and dry conditions. The radar backscatter σ of winter multiyear sea-ice was set to -9 dB at 23° for C-band VV-polarization (Kwok and others, 1992), -15 dB at 35° for L-band HH-polarization (Ulaby and others, 1986), and to -28 dB at 35° for P-band HH-polarization (Parashar, 1974). As a result of natural spatial variations in radar backscatter from multi year sea-ice, and temporal variations induced by changing environmental conditions, these reference values have a standard deviation of 2.2 dB at C-band, 2 dB at L-band (Kwok and others, 1992; Rignot and Kwok, 1993), and 2 dB at P-band (Parashar, 1974).

4. WEATHER AND ICE CONDITIONS

Weather data were collected within a 150 km radius at the APLIS'88 ice station located approximately 350 km North of Prudhoe Bay, Alaska, between March and April 1988 (Wen and others, 1989). These data provide the most reliable information about the meteorological conditions in the region where the SAR imagery were acquired. Daily observations of air-temperatures, atmospheric pressure, and wind direction and speed collected at APLIS'88 are summarized in Figure 3. Air-temperatures were below -10°C on March 11, rose to about -7°C, and subsequently fell below -20°C on March 19. Wind speeds were usually below 5 m/s. Measurements of the drift speed

of the ice station (Wen and others, 1989) revealed rapid ice motion and deformation on March 10 correlated with high wind speeds of 7-8 m/s. Sea-ice images of March 11 (Fig. 1) reveal important new cracks and leads in the ice created by divergent ice motion, with leads rapidly freezing under the cold conditions. The newly frozen ice leads remained relatively undeformed indicating that little convergence was observed after freeze-up. Significant deformation is however revealed in first-year ice surrounding the large and rounded multiyear ice floes with the presence of a dense and complex network of rubble fields and ridges over the whole area. Ice conditions at APLIS'88 (Fig. 2) comprised a mixture of first-year ice, and multiyear ice floes (Cavalieri and others, 1991). The ice camp was located at the edge of a multiyear ice floe, near a smooth and undeformed refrozen lead which was used to build an aircraft runway. First-year ice in the vicinity of the station was 1.5 m to 2.4 m thick, with a dry snow cover of variable depth with a mean of 15 cm, and a relatively flat surface. Wen and others (1989) reported that multiyear ice floes were snow-covered and hummocked to amplitudes of 6 m. Pressure ridges and rubble fields fringed the lead near the camp. Immediately North of the lead was a relatively rough rubble field with large ice chunks. An aerial photo of the ice camp looking North (Fig. 4) shows the boundaries of multiyear ice floes, deformed and rough first-year ice, and refrozen lead. An aerial photo looking South (Fig. 5), reveals the hummocky surface of the large multiyear ice floe at the edge of the ice camp, and zones of deformed first-year ice. Examination of the underside topography by divers revealed a large spatial variability in the growth rate of first-year ice, and large differences in bottom roughness features from those of multiyear ice where rounded and polished keels with no block structure contrasted with the young keels comprising randomly oriented blocks of ice in first-year ice. Ice cores taken from the smooth FY ice in the lead to estimate temperature, salinity, density, and brine volume profiles (Fig. 6) revealed

the recently-grown ice to be columnar in structure.

5. SELECTION AND LABELING OF THE ICE TYPES

Selecting a set of physically relevant sea-ice types from remotely sensed imagery is difficult because: 1) the nomenclature of ice types is based on physical properties such as ice thickness, age, formation history, and surface roughness, which do not provide a unique relationship between ice types and radar backscatter; 2) the microwave properties of sea-ice vary widely with seasonal temperature (Onstott and Gogineni, 1985; Onstott and others, 1987; Cavalieri and others, 1990) and geographical location (Livingston and others, 1987); and 3) *in-situ* surface observations, when available at all because of technical difficulties and costs of operation, are limited to sparse point measurements at the surface which do not provide enough spatial details compared to the remotely sensed imagery. A standard procedure is to identify visually certain ice conditions present in the imagery, select training areas representative of each ice type, extract their microwave signatures, and then classify each image pixel into these ice conditions. This supervised procedure provides confidence in the results, and attempts at minimizing classification errors, but requires detailed independent surface information (lacking due to expense and logistical difficulty), and homogeneous ice areas across swath, containing many pixels, and with clear and well defined boundaries. As the dimensionality of the remotely sensed data increase (with polarimetry and multifrequency), and the complexity of the scene features increase (in deformed first-year ice), manual selection of relevant ice classes becomes rapidly difficult and randomized,

Instead, we selected ice classes using an unsupervised clustering technique because it is nearly automatic; needs no training areas; provides a non-subjective characteriza-

tion of unique and separable classes of radiometric and polarimetric radar backscatter; and often performs a more sensitive selection of the mean cluster characteristics, because selection is a computer optimized process. We used the clustering technique developed by Rignot and others (1992a) for multi-parameter SAR data. To account for variations in radar backscatter from each ice type due to changes in the incidence angle θ_i across the swath, we separated each SAR scene into 3 distinctive regions, so that within each region changes in radar backscatter with θ_i of each ice type are less than their expected separability in radar backscatter; followed by a cluster analysis of L- and C-band polarimetric data in each region. The 3 regions correspond in Image 1372 to: 1) $29^\circ \leq \theta_i \leq 36^\circ$; 2) $36^\circ \leq \theta_i \leq 45^\circ$; 3) $\theta_i \geq 45^\circ$; and in Image 311 to: 1) $20^\circ \leq \theta_i \leq 29^\circ$; 2) $29^\circ \leq \theta_i \leq 41^\circ$; 3) $\theta_i \geq 41^\circ$. The cluster analysis routine was initialized with an expected number of clusters equal to 6 for Image 311 separated by at least 4 dB, and to 7 for Image 1372 (thin ice is an additional ice type present in Image 1372) separated by 4 dB. A 4 dB minimum separation in radar backscatter corresponds to a theoretical classification error of the image pixels of less than 1 % (Rignot and Chellappa, 1991). The final number of clusters, which is not bound to the initial guess, was 6 for Image 311 and 8 for Image 1372. The radar backscatter characteristics of the clusters are given in Table 1 and 2. We labeled the clusters into 6 different sea-ice types (open water is absent from the data), thereby regrouping some of the clusters together into a single ice type. This regrouping of clusters is expected to be part of the selection process as clustering provides image classes independent from the fact that they may or may not share similar geophysical characteristics. Several clusters are expected in first-year ice because of the large dynamic range in radar backscatter of first-year ice due to spatial changes in small-scale surface roughness, and the presence of pressure ridges and rubble fields. Multiple clusters are also expected in multiyear ice due to the variety of constituents that contribute to

its radar signatures, including multiyear smooth/flat ice, hummocks, pressure ridges, and melt-pools (Onstott, 1992). Independently in each region, each image pixel was subsequently classified into one of these ice classes using a Maximum A Posteriori (MAP) Bayesian classifier for multi-parameter SAR data described in Rignot and Chellappa (1992b). The resulting sub-images were reconstituted, and matching was found to be excellent at the boundaries. P-band was not used because it is similar to L-band and reduces the classification quality for thin ice of low backscatter. The 6 identified ice conditions are labeled in the following fashion (Fig. 1c and 2c): 1) old compressed first-year ice (CFY); 2) first-year rubble and ridges (FYRR); 3) multi-year ice (MY); 4) first-year rough and deformed ice (FYR); 5) first-year smooth and undeformed ice (FYS); and 6) thin first-year ice (ThI).

Figure 7 shows examples of radar backscatter curves for the 6 ice types present in image 1372. The plotted values were obtained for each ice type by averaging along each range line (same incidence angle) the radar backscatter values of all the pixels classified into that particular ice type (Fig. 1c), and smoothing the results using a ten points moving window. The curves illustrate the separability between the different ice types at HH- and HV-polarization versus θ_i . At C-band, MY and CFY are confused, except from a small contrast at HV-polarization, but MY and FY are separated by several dB. The continuity of the curves at the transition between different regions confirms that matching of the sub-images is satisfactory. The radar backscatter curves at L-band are consistent with published scatterometer measurements (Fig. 2 Onstott and others, 1982), including the more rapid decay of MY with θ_i at HH-polarization compared to FY (Fig. 5 Onstott and others, 1979). Radar backscatter values at HV-polarization are less sensitive to θ_i because volume scattering effects dominate the radar returns,

Figure 1 d shows the brightness temperatures of the ice obtained from airborne passive microwave data acquired by NORDA's K_a -band (33.6 GHz) Radiometric Mapping System (KRMS) (Eppler and others, 1986) at the same location as Image 1372. KRMS data were not available for Image 311. The KRMS data were calibrated using the procedure described in Farmer and others (1990), and were resampled and projected into slant-range to facilitate inter-comparison with the slant-range SAR data. The spatial resolution of the KRMS data is 145 m in the center of the swath, decreasing towards the edges of the swath with increasing geometric distortions. Because of residual calibration errors and geometric distortions, the KRMS imagery is only used here to indicate the presence of certain ice-types, and not as a validation procedure of the SAR results per-se. Nevertheless, the brightness temperatures T_B together with the contextual information clearly indicate the presence of multiyear ice (MY), first-year ice (FY), and thin ice (ThI); although MY is not well separated from ThI by T_B alone (Table 3). MY is colder than FY. ThI is the coldest, but not cold enough to correspond to open water since $T_B = 141 K \pm 1 K$ for calm and cool open water (Eppler, private communication, 1992),

ThI is distinguished in Image 1372 by its low radar backscatter at all frequencies, and by the obvious presence of a recently frozen lead in the center of the scene consistent with the ice drift and divergence recorded in the near-by ice camp on March 10. The polarimetric characteristics of ThI at L-band provide evidence that it does not contain any open water. The small perturbation model (SPM) (Lice, 1951) predicts that for slightly rough surfaces the ratio $\gamma = \sigma_{VV}/\sigma_{HH}$ increases with the incidence angle θ_i and the real part of the dielectric constant ϵ_r of the surface, independent of the rms height of the surface at the wavelength scale. Since ϵ_r increases with ice salinity, γ is expected to be larger in young thin FY ice, than in thick FY ice, and indeed

MY ice; and is largest in open water. Assuming SPM applicable to smooth sea-ice at L-band (Winebrenner and others, 1989), we inverted γ of the pixels classified as ThI in Image 1372 (Fig. 1c) for ϵ_r . The histogram of ϵ_r values is shown in Figure 8. System noise power level estimates were used to correct γ from the bias introduced by system noise in thin ice of low backscatter. ϵ_r of ThI is large in average, yet much lower than that expected for open water ($\epsilon_r = 80$) for which SPM is applicable when the wind speed is low and the rms height of the water surface is typically less than one tenth of the wavelength (Kim and others, 1992). If open water were present in the ThI lead, its surface would have to be very smooth because the radar backscatter values recorded in the lead are very low. Assuming an ice temperature of -5°C (no snow cover was present on ThI, and the air-t temperature was -10°C), an ice density of 0.75 g/cm^3 , and using the dielectric mixing formulae of Vant and others (1974 and 1978) and the phase relations for sea-ice of Stogryn and Desargent (1985), we estimated the salinity of ThI to be greater than 68 ppt for ϵ_r larger than 6, indicating that most of the thin ice within the lead probably included large quantities of brine, some perhaps even in slush or liquid form at the surface. The large spread of ϵ_r values suggests large unhomogeneities within the lead. These results are consistent with a lead formation a day or so prior to flight, followed by a rapid freeze-up due to the cold-air temperatures (Fig. 3). Ice thicknesses were likely in the few cm range. We did not perform a similar inversion at C-band because γ offers less contrast between ThI ice and open water, roughness effects become significant at shorter wavelengths, and SPM no longer applies (Kim and others, 1992).

Labeling MY ice is facilitated by the highly recognizable rounded shape of MY floes, their cold brightness temperatures in the KRMS data in Image 1372, and their existence at the ice camp. The boundaries of MY ice floes appear distinctly in the aerial

photos (Fig. 4 and 5) due a sharp transition in surface roughness, and in the 1,-band III imagery (Fig. 1b and 2b) due to a sharp transition in radar brightness. MY in Image 1372 has radar backscatter characteristics that are similar to those measured in Image 311 (Table 1 and 2), An exception is the large fragmented MY ice floe in the center of Image 3]] which includes numerous patches of CFY which correspond to the hummocks and ridges reported in Wen and others (1 989), and the features visible in Fig. 5.

FYRR comprises extensive pressure ridges and rubble fields of broken blocks of upstanding ice in the highly deformed FY ice present in the 2 scenes (Fig. 4 and 5). Ridges are geophysically important because they have a major influence on the drag coefficient of the surface (Burns, 1990), and they account for a significant portion of the total ice mass, FYR is also rough deformed FY ice, but does not include pressure ridges, and is less deformed and less rough than FYRR. Manninen (1991) showed using radar backscatter model predictions that differences in radar backscatter from deformed FY ice are mostly due to differences in small scale surface roughness as opposed to differences in dielectric constant and ridge structure. Breaking rough first-year ice into two distinct classes is relevant in our context because MY has an intermediate range of radar backscatter at 1,-band between FYR and FYRR (Fig. 7c), whereas MY is consistently brighter than both ice types at C-band (Fig. 7a and b). Hence, FYRR is likely to be misclassified as MY ice at 1,-band. FYS is another FY ice type that is easily identified due to its existence at the location of the aircraft runway in Image 311, and its low radar backscatter in Image 1372 and 311, indicating a smoother surface at the wavelength scale.

CFY is particularly interesting because C-band signals clearly mix it with MY ice

whereas L-band signals mix it with FY ice. No salinity profile was acquired at that particular location to establish on a strong basis that CFY is indeed FY ice; but examination of aerial photos, KRMS data, and polarimetric SAR characteristics concur to indicate that CFY is younger ice than the MY ice which it glues together. The brightness temperature of CFY is 16 K warmer than that of h4Y ice although not as warm as the other types of FY ice, indicating an ice type younger than MY ice, CFY ice coincides with highly deformed surfaces consisting of large uplifted ice blocks both within and surrounding MY ice floes (Fig. 4 and 5), clearly generated by compression and shear forces during ice drifting, indicating that CFY is very deformed FY ice that surrounds and holds together the MY floes, In both Table 1 and 2, ρ_{HHVV}^* is about 0.7 for FY ice at L-band, 0.9 for MY ice, and 0.7 for CFY ice. A higher correlation between HH and VV is expected in MY which exhibits azimuthal symmetry and for which scatterers are isotropically distributed (Nghiem and others, 1992). In contrast, first-year ice has preferential vertical structures observed in the orientation of brine inclusions (Weeks and Ackley, 1982), yielding lower values of ρ_{HHVV}^* because HH and VV signals are not sensitive to the same saline inclusions and thereby the same scatterers. A lower ρ_{HHVV}^* in CFY at L-band indicates more pronounced heterogeneities in salinity in CFY than in h4Y ice, and hence a younger ice type. Finally, the higher radar backscatter of CFY at L- and C-band compared to other types of FY ice suggests a much rougher surface, consistent with the hypothesis that CFY has an extremely rough surface comprised of blocks of FY ice from ice pushed up and uplifted around the edges of the larger, thicker, and more massive h4Y ice floes. CFY is not distinguished from h4Y at C-band, except for a 1-2 dB contrast at HV-polarization. Multiple surface scatter from this lower salinity CFY, (because of uplift and drainage) together with penetration and volume scatter from voids between blocks, could explain microwave signatures equivalent to that of smooth MY

at C-band.

The classification error of the ice maps (Fig. 1c and 2c) is difficult to estimate in the absence of ground truth information on a pixel by pixel basis, as typical of most polar remote sensing experiments. Errors due to the classifier itself are negligible due to the large contrast between ice types. Classification performance is therefore only limited by system errors (interferences, processing artifacts), and by confusion of certain ice types by the radar. In Image 1372, FY is misclassified as MY in one line running from top to bottom in the center of Fig. 1 c because of the corrupting influence of system interference in the C-band H- received channel. These errors do not appear in Fig. 9c since C-band H- received channel is not used. In both Image 311 and Image 1372, small patches of FY ice are detected within MY ice floes that could correspond to melt ponds. Refrozen melt ponds are perhaps misclassified as FY ice by the radar because the surface is likely very smooth and bubble free. Similarly, a number of MY floes include segments of CFY ice which may correspond to MY pressure ridges or hummocks and are therefore misclassified as FY ice. MY pressure ridges are typically composed of blocks of ice with tilted surfaces that produce strong backscatter due to scattering from individual facets, multiple facet scattering, and in some cases enhanced volume scattering due to a transition to a very low density ice form (Onstott, 1992), so that they may share common scattering characteristics with CFY ice. Except for the case of the large MY floe in the center of Image 311 which is obviously fragmented and held together by large patches of CFY, CFY ice in the midst of MY ice floes should really be classified as MY ice, while CFY ice surrounding the MY ice floes and holding them together is not MY ice. By counting all the misclassified pixels discussed above, we estimated the classification accuracy of the ice maps to be greater than 90%. Gray and others (1982) reported similar

classification accuracies combining scatterometer and radiometer data acquired over the Beaufort sea in March-April 1979 to separate 6 ice conditions. In this study, only the radar data are used to separate these ice types.

6. CLASSIFICATION ACCURACY VS FREQUENCY AND POLARIZATION

The ice map obtained using L- and C-band polarimetric combined (Fig. 1c) is used as a reference map of the ice types present in the scene, and ideally for the present time its classification accuracy is assumed to be 100%. Reclassified images are then generated using a reduced number of polarizations and frequencies, and a relative classification accuracy of each ice type is computed in reference to the classification map in Fig. 1c and then recorded in confusion matrices. A representative sample of the confusion matrices obtained for each test case is given in Table 4 for Image 1372 with $\theta_i \geq 45^\circ$. Each confusion matrix indicates how classification inaccuracy results in rebinning of pixels in the wrong ice classes, along with the percentage of misclassified pixels. Vertical columns indicate how for a particular ice class, various pixels are misclassified. Each vertical column totals 100%, and components of each vertical column denote the percentage of misclassification (as other classes) relative to the results in Fig. 1c. An overall relative classification accuracy of each combination of parameters is computed from the average of the diagonal elements in each of the confusion matrices. These confusion matrices are computed from all the pixels included in the image. FYRR and FYR are regrouped into one ice class denoted FYR as both correspond to deformed FY ice but with a larger variance.

At C-band, a large contrast in radar backscatter exists between MY and undeformed FY (Fig. 7) due to the additional volume backscatter of the low density bubble-

rich layer contained in the upper part of the MY sea-ice (Kim and others, 1984). Yet, C-band VV-polarization alone achieves only 67% overall relative classification accuracy (Table 4a), as MY and CFY are not separated. C-band HV-polarization better separates MY and CFY, and MY from FY, but confuses ThI and FYS, yielding a 69% classification accuracy (Table 4b). C-band HH-polarization has a relative classification accuracy of 71%. C-band HH- and HV-polarizations combined increase the C-band VV-polarization results by 10% (Table 4c). Other combination of two polarimetric channels yield similar relative accuracies (Table 4d). The best results are obtained with the complete polarimetry (Table 4e), but two polarizations perform nearly as well and significantly better than single-polarization.

The contrast between MY and FY is reduced at L-band (Fig. 7) because MY generates almost no additional volume scattering (Winebrenner and others, 1989). Classification accuracy is 75% at L-band HH-polarization because MY is confused with FYR and CFY (Table 4f), confirming that L-band at one polarization is not useful for ice mapping (Lyden and others, 1984; Onstott and others, 1982). Two like-polarization channels however improve the relative accuracy by 9% (Table 4g). The full polarimetry does not improve the results and actually yields a 1% drop in accuracy because the HV radar returns increase confusion between MY and FYR (Table 4h, and Fig. 7d). This example demonstrates that increasing the number of channels does not necessarily increase classification accuracy in a polarimetric classifier. Notwithstanding this observation, L-band performs better than C-band over all classes when more than one polarization is used, despite the reduced contrast between MY and deformed FY ice.

P-band is similar to L-band with a reduced contrast between MY and FY. Although

P-band is not considered as particularly useful for ice mapping (Parashar and others, 1977), the classification results are described here for sake of completeness. The classification accuracy is 60% at HH-polarization, 70% at HH- and VV-polarizations combined (Table 4i), and only 58% with the full polarimetry (Table 4j). The HH backscatter confuses several ice types resulting in a relative accuracy of 48% when used alone, and in a poor performance of the full polarimetry.

Finally, the classification accuracy combining two frequencies at one polarization is investigated. L-band H-polarization and C-band VV-polarization have an overall relative accuracy of 90% (Table 4k), which is better than any fully polarimetric single frequency or indeed any non-polarimetric single frequency. Other combinations using L- and C-band at a single polarization yield similar results (Table 4l). To summarize, Figure 9 shows ice maps of Image 1372 over the entire range of incidence angle at C-band VV, L-band HH, L-band HH and C-band VV combined, and L-band polarimetric. MY and CFY have the same color at C-band VV (Fig. 9a) because they are not separated. Floe boundaries are not distinguishable, and the MY ice fraction is clearly overestimated. This classification result, which uses the same image as in Kwok and others (1992), illustrates the inaccuracies inherent to a C-band ice classification scene in a transition zone where CFY is present in large quantities. At L-band HH (Fig. 9b), MY floe boundaries appear clearly, but many ice pixels in deformed FY ice are misclassified as MY ice. Combining the two frequencies yields a large improvement in classification accuracy, and the ice map (Fig. 9c) even compares favorably to the one in Fig. 1 c since errors induced by system interference are eliminated. This result shows that ice mapping could improve significantly by combining ERS-1 and JERS-1 SAR data, assuming that both sensors could image the same area at the same time. MY ice floe boundaries appear distinctly, MY is well separated from CFY, and

the distribution of ridges can be extracted. The results obtained using L-band polarimetry (Fig. 9d) confirm that polarimetry is more useful at L-band than at C-band for ice mapping (Table 4c,h), and Table 4g shows that only two channels are needed at L-band to yield classification accuracies only 7% lower than that obtained using L- and C-band polarimetric.

7. COMPARISON OF ICE FRACTION ESTIMATES

Ice maps generated from SAR data can be used to provide estimates of the old ice fraction, the thick ice fraction for freshwater budget calculations, and the thin ice fraction for area heat-flux estimates. Table 5 shows estimates of the old, thick, and thin ice fractions computed using various frequencies and polarizations, CFY is regrouped with MY for estimation of the thick ice fraction as CFY may correspond to extremely thick FY, possibly as thick as MY because of compression, ridging, and uplifting (Johansson and Askne, 1987). At C-band VV, the old ice fraction is overestimated by 15%. Based on the ice map shown in Fig. 9a, the error is even larger for $\theta_i \leq 30^\circ$ which corresponds to the imaging conditions of ERS-1 SAR. In contrast, the thick ice fraction is estimated with less than 3% error. Hence ERS-1 may overestimate the old ice fraction in transition zones where CFY is present, but may provide reliable estimates of the thick ice fraction. Similar results are obtained at C-band HH, suggesting that RADARSAT will suffer the same drawbacks as ERS-1 SAR. At L-band single-polarization, both the old and thick ice fractions are largely misestimated. The addition of one other polarization provides however good estimates of both the old (0.70 error compared to the last column of Table 5, and little confusion in Table 4g) and thick ice fractions (4% error in Table 5, and little confusion in Table 4h). Better results are obtained combining L- and C-band at one polarization.

Combining SAR data from ERS-1 and JERS-1 should improve the estimation of ice fractions significantly compared to that obtained using each sensor separately. The thin ice fraction is in general correctly estimated at both L- and C-band. C-band VV-polarization slightly overestimates it compared to C-band HH-polarization because the contrast between FYI and THI is 2 dB smaller at C-band VV (Table 1 and 2). L-band VV-polarization overestimates the thin ice fraction compared to L-band HH-polarization for the same reason.

8. CONCLUSIONS

This paper presents examples of quantitative improvements in classification accuracy of 6 winter ice conditions using SAR data resulting from the combination of multiple polarizations and frequencies. The indications are that 10% improvement in classification accuracy results from the use of two polarizations instead of a single polarization. Single frequency full polarimetry does not significantly add to classification accuracy. Simply, combining two frequencies (L- and C-band) at a single polarization improves classification accuracy by 10 to 20%, but the addition of a third frequency (P-band) does not necessarily improve the results. Two frequencies (L- and C-band) and two polarizations perform as well as L-, C-, and P-bands fully polarimetric combined, in terms of separating the ice conditions discussed in this paper. Finally, polarimetric information is more useful at L-band than at C-band for winter ice mapping, and for separating thin ice from calm open water,

Other frequencies have been suggested in the past, such as X-band (Parashar and others, 1977; Onstott and others, 1979 and 1982; Kim and others, 1984), for better discrimination between FYI and MYI. They have not been considered in this paper because they were not available, and because L- and C-band are the only

two frequencies available from space over the polar regions for a number of years to come, and we need to establish clearly the level of performance of these different SAR systems for ice mapping. Our results suggests that deformed FY ice plays a critical role in the interpretation of microwave signatures of sea-ice, and in mapping of ice conditions, even in winter when MY and undeformed FY are well separated in radar backscatter; but that these ambiguities can be resolved by combining L- and C-band data. Further studies, validation campaigns, and intra-sensor comparisons should intensify current efforts to relate the radar backscatter characteristics and emission properties of deformed FY ice to their physical properties at various wavelengths to help resolve differences in ice fraction estimates obtained from different remote sensing techniques (Cavalieri and others, 1991; Rothrock, 1991).

Acknowledgement: E. R., and M. J. performed this work in the Aircraft Radar Group of the Radar Science and Engineering Section and in the Polar Oceanography Group at the Jet Propulsion Laboratory, California Institute of Technology, under contract to the Oceanic Processes Branch of the National Aeronautics and Space Administration. The authors wish to thank Duane Eppler and Dennis Farmer for use of the KRMS image data, and Timothy Wen for providing us with pictures of the APLIS88 camp.

REFERENCES

- Attema, E. P. W. 1991. The active microwave instrument on-board the ERS-1 satellite, *Proc. IEEE*, 79, 791-799.
- Burns, B.A. 1990, SAR image statistics related to atmospheric drag over sea-ice, *IEEE Trans. Geosc. and Rem. Sens.*, 28(2), 158-165.
- Borgeaud, M., R. T. Shin, and J. A. Kong. 1987, Theoretical models for polarimetric radar clutter, *J. Electrom. Waves and Applic.*, 1(1), 67-86.
- Bredow, J. S., S. P. Gogineni, A. J. Gow, P. F. Blanchard, and R. K. Moore, 1989. Radar backscattering from artificially grown sea-ice, *IEEE J. Oceanic Eng.*, 14, 259-264.
- Carsey, F. 1989. Review and status of remote sensing of sea-ice, *IEEE J. Oceanic Eng.*, 14(2), 127-138.
- Cavalieri, D. J., B. A. Burns, and R. G. Onstott. 1990. Investigation of the effects of summer melt on the calculation of sea-ice concentration using active and passive microwave data, *J. Geophys. Res.*, 95(C4), 5339-5369.
- Cavalieri, D. J., J. P. Crawford, M. R. Drinkwater, D. T. Eppler, L. D. Farmer, R. R. Jentz, and C. C. Wackerman. 1991. Aircraft active and passive microwave validation of sea-ice concentration from the Defense Meteorological Satellite Program Special Sensor Microwave Imager, *J. Geophys. Res.*, 96(C12), 21989-22008.
- Drinkwater, M. R., R. Kwok, D. P. Winebrenner, and E. Rignot. 1991. Multi-frequency polarimetric SAR observations of sea-ice. *J. Geophys. Res.*, 96(C11), 20679-20698.
- Eppler, D. T., L. D. Farmer, A. W. Lohanick, and M. Hoover. 1986. Classification of ice types with single band (33.6 GHz) airborne passive microwave imagery, *J. Geophys. Res.*, 91(C9), 10,661-10,695.
- Farmer, L.D., D.T. Eppler, and A.W. Lohanick. 1990. Converting digital passive microwave radiances to Kelvin units of brightness temperatures, *NORDA Tech. Note*, 427, 17 pp., NORDA, Stennis Space Center, MI.
- Fily, M. and D. A. Rothrock. 1990, Opening and closing of sea-ice leads: Digital measurements from synthetic aperture radar, *J. Geophys. Res.*, 95(C1), 789-796.

Freeman, A. 1990. A calibration and image quality assessment of the NASA/JPL aircraft SAR during Spring 1988, *JPL Tech. Rep., D-7197*, 60 pp., Jet Propul. Lab., Calif. Inst. of Technol., Pasadena.

Gray, A. L., R. K. Hawkins, C. E. Livingstone, L. Drapier Arsenault, and W. M. Johnstone. 1982, Simultaneous scatterometer and radiometer measurements of sea-ice microwave signatures, *IEEE J. of Oceanic Eng.*, 7, 20-32.

Johansson, R. and J. Askne. 1987. Modeling of radar backscattering from low-salinity ice with ice ridges, *Int. J. Rem. Sens.*, 8(11), 1667-1677.

Kim, Y. S., R. K. Moore, and R. G. Onstott. 1984. Theoretical and experimental study of radar backscatter from sea-ice, *Remote Sensing Lab.*, Univ. of Kansas, Lawrence, KS, Tech. Rep. 331-37.

Kim, Y., E. Rodriguez, and S. Durden. 1992. A numerical assessment of rough surface scattering theories: vertical polarization) *Radio Science*, 27, 515-528.

Kwok, R., J. C. Curlander, R. McConnell, and S. Pang. 1990. An ice motion tracking system at the Alaska SAR Facility, *IEEE J. Oceanic Eng.*, 15(1), 44-54.

Kwok, R., E. Rignot, B. Holt, and R. G. Onstott. 1992. Identification of ice types in spaceborne synthetic aperture radar data, *J. Geophys. Res.*, 97(C2), 2391-2402.

Livingstone, C. E., K. P. Singh, and A. L. Gray. 1987. Seasonal and regional variations of active/passive microwave signatures of sea-ice, *IEEE Trans. Geosc. and Rem. Sens.*, 25(2), 159-173.

Lyden, J. D., B. Burns, and A. L. Maffet. 1984. Characterization of sea-ice types using synthetic aperture radar, *IEEE Trans. Geosc. Electron.*, 22(5), 431-439.

Manninen, A. T. 1991. Surface backscattering dependence on various properties of ice ridges, in Proceedings, IGARSS'91, Vol. 3, *Cat. No. 91 CH2971-0*, 1219-1226, IEEE, New York.

Nemoto, Y., H. Nishino, M. One, H. Mizutamari, K. Nishikawa, and K. Tanaka. 1991. Japan Earth Resources Satellite- 1 synthetic aperture radar, *Proc. IEEE*, 79, 800-809.

Nghiem, S. V., S. H. Yeh, R. Kwok, and F. K. Li. 1992. Symmetry properties in polarimetric remote sensing, *Radio Sci.*, 27, 693-712.

Onstott, R. G., R. K. Moore, and W. F. Weeks. 1979. Surface-based scatterometer results of Arctic sea ice, *IEEE Trans. on Geosc. Electron.*, **17**(3), 78-85.

Onstott, R. G., R. K. Moore, S. Gogineni, and C. V. Delker. 1982. Four years of low altitude sea ice broadband backscatter measurements, *IEEE J. Oceanic Eng.*, **7**(1), 44-50.

Onstott, R. G., and S. Gogineni. 1985. Active microwave measurements of Arctic sea-ice under summer conditions, *J. Geophys. Res.*, **90**(C3), 5035-5044.

Onstott, R. G., T. C. Grenfell, C. Mätzler, C. A. Luther, and E. A. Svendsen. 1987. Evolution of the microwave sea-ice signatures during early summer and midsummer in the marginal ice zones, *J. Geophys. Res.*, **92**(C7), 6825-6835.

Onstott, R. G. 1992. SAR and scatterometer signatures of sea-ice, in *Microwave Remote Sensing of sea-ice; Chapter 5*, (Carsey and others, Eds), The American Geophysical Union, Washington 1). C., pp. 73-102.

Parashar, S. K. 1974. investigation of radar discrimination of sea ice, Ph.D. Dissertation, The University of Kansas, Lawrence, KS.

Parashar, S. K., R. M. Haralick, R. K. Moore, and A. W. Biggs. 1977. Radar scatterometer discrimination of sea ice types, *IEEE Trans. on Geosc. and Electron.*, **15**(2), 83-87.

Raney, R. K., A. P. Luscombe, E. J. Langham, and S. Ahmed. 1991. RADARSAT, *Proc. IEEE*, **79**, 827-838.

Rice, S. O. 1951. Reflection of electromagnetic waves from slightly rough surfaces, *Commun. Pure Appl. Math.*, **4**, 351-378.

Rignot, E. and R. Chellappa. 1991. Segmentation of complex synthetic aperture radar data, *J. Opt. Soc. Am.*, **A8**, 1499-1511.

Rignot, E., R. Chellappa, and P. Dubois. 1992a. Unsupervised segmentation of polarimetric SAR data using the covariance matrix, *IEEE Trans. Geosc. and Rem. Sens.*, **30**(4), 687-705.

Rignot, E. and R. Chellappa. 1992b. Segmentation of polarimetric SAR data, *IEEE Trans. Image Proc.*, **1**, 281-300, 1992b.

Rignot, E. and R. Kwok. 1993. Characterization of spatial statistics of distributed

targets in SAR data, *Int. J. of Rem. Sens.*, 14, 345-366.

Rothrock, D. A. 1991. Ice thickness observations from satellites, *Report of the sea ice thickness Workshop, 19-21 Nov. 1991*, New Carrollton, Maryland, Thorndike and others, Edts., Applied Physics Lab., Univ. of Washington, Seattle, Washington, pp. 60-64.

Tsang, L. and J. A. Kong. 1981. Scattering of electromagnetic waves from random media with strong permittivity fluctuations, *Radio Sci.*, **16**, 303-320.

Tsang, L., and A. Ishimaru. 1987. Radiative wave equations for vector electromagnetic propagation in dense nontenuous media, *J. Electromagn. Waves Appl.*, 1(1), 59-72.

Ulaby, F. T., R. K. Moore, and A. K. Fung. 1986. *Microwave Remote Sensing: Active and Passive*, vol. 111, Artech House, Dedham, MA.

Ulaby F. T. and C. Elachi. 1990. *Radar Polarimetry for Geoscience Applications*, F.T. Ulaby and C. Elachi Edts, Artech House Inc., Norwood, MA.

van de Hulst, H. C. 1981. *Light scattering by small particles*, Dover, New York, pp. 28-42.

van Zyl, J. J. 1990. Calibration of polarimetric radar images using only image parameters and trihedral corner reflector responses, *IEEE Trans. Geosc. and Rem. Sens.*, 28(3), 337-348.

Vant, M. R., R. B. Gray, R. O. Ramseier, and V. Makios. 1974. Dielectric properties of fresh and sea ice at 10 and 35 GHz, *J. Appl. Phys.*, **45**, 4712-4717.

Vant, M. R., R. O. Ramseier, and V. Makios. 1978. The complex dielectric constant of sea-ice at frequencies in the range 01.-40 GHz, *J. Appl. Phys.*, **49**, 1264-1280.

Weeks, W. F. and S. F. Ackley. 1982. *The Growth, structure, and properties of sea-ice*, *CRREL Monogr. 82-1*, 130 pp., US Army Cold Reg. Res. and Eng. Lab., Hanover, N. H.

Wen, T., W. J. Felton, J. C. Luby, W. L. Fox, and K. L. Kientz. 1989. Environmental measurements in the Beaufort sea, Spring 1988, *Tech. Rep., A PL-UW TR 8822*, **34** pp., Appl. Phys. Lab., Univ. of Wash., Seattle.

Winebrenner, D. P., L. Tsang 1., B. Wen, and R. West. 1989. Sea ice characteriza-

tion measurements needed for testing of microwave remote sensing models, *IEEE J. Oceanic Eng.*, 14(2), 147-157.

LIST OF TABLES

TABLE 1. Table of the polarimetric characteristics of the cluster centers of Image 1372 for $\theta_i \geq 45^\circ$ at L-, and C-band frequencies, along with their sea-ice label. σ_{XY} is the radar backscatter at XY-polarization expressed in dB, ρ_{HHVV}^* is the magnitude of the correlation coefficient between the HH and VV returns expressed in linear units, and ϕ_{HHVV}^* is the mean phase difference between the HH and VV returns expressed in degrees. The noise power level at HH and VV polarizations, and $\theta_i = 45^\circ$, is -44 dB at L-band and -40 dB at C-band, The values of ρ_{HHVV}^* are not corrected from biases introduced by system noise.

Frequency	σ_{HH}	σ_{HV}	σ_{VV}	ϕ_{HHVV}^*	ρ_{HHVV}^*	Ice Label
L-	-33.9	-41.6	-27.8	-1	0.57	ThI
	-26.5	-38.6	-23.6	-10	0.71	FYS
	-21.7	-33.4	-19.3	-7	0.74	FYR
	-19.2	-33.9	-16.2	0	0.91	MY
	-17.7	-27.5	-15.7	-3	0.74	FYR
I	-16.1	-26.2	-13.6	0	0.80	MY
	-14.1	-24.0	-12.3	0	0.74	FYRR
	-11.8	-19.6	-9.8	1	0.71	CFY
C-	-29.8	-36.6	-27.1	8	0.39	ThI
	-22.9	-35.3	-22.9	7	0.66	FYS
	-21.3	-33.7	-21.0	8	0.70	FYR
	-13.0	-23.0	-12.0	2	0.70	MY
	-19.5	-31.6	-19.1	10	0.71	FYR
	-12.3	-21.3	-11.4	1	0.63	MY
	-16.9	-28.3	-16.6	13	0.70	FYRR
	-12.4	-20.9	-11.6	8	0.58	CFY

TABLE 2. Table of the polarimetric characteristics of the cluster centers of Image 311 for $\theta_i \geq 41^\circ$ at L-, and C-band frequencies, along with their sea-ice type labeling. Notations are the same as in TABLE 1.

Frequency	σ_{HH}	σ_{HV}	σ_{VV}	ϕ_{HHVV}^*	ρ_{HHVV}^*	Ice Label
L-	-26.2	-42.0	-23.7	3	0.73	FYS
	-20.7	-31.6	-17.9	1	0.75	FYR
	-20.6	-36.4	-17.4	7	0.90	MY
	-17.7	-34.1	-15.6	6	0.90	MY
	-15.8	-25.2	-13.1	3	0.75	FYRR
	-12.9	-21.3	-10.4	5	0.71	CFY
C-	-22.2	-31.9	-23.7	1	0.65	FYS
	-19.6	-27.2	-20.2	1	0.64	FYR
	-13.8	-20.7	-13.8	2	0.71	MY
	-12.7	-19.6	-12.8	2	0.72	MY
	-14.3	-20.4	-14.6	2	0.67	FYRR
	-11.9	-17.1	-12.3	2	0.61	CFY

TABLE 3. Table of brightness temperature T_B (in K) and standard deviations σ_{T_B} of 5 ice types in Image 1372,

Ice Type	$T_B \pm \sigma_{T_B}$
ThI	150 ± 13
FYS	208 ± 3
FYR	217 ± 2
MY	156 ± 3
CFY	182 ± 5

TABLE 4. Confusion matrices of five ice types at, (a) C-band VV; (b) C-band HV; (c) C-band HH and HV; (d) C-band 1111 and VV; (e) C-band full polarimetry; (f) L-band HH; (g) L-band HH and VV; (h) L-band full polarimetry; (i) P-band HH and VV; (j) P-band full polarimetry; (k) L-band HH and C-band VV; (l) L-band HV and C-band HH.

(a)

Ice Type	ThI	FYS	FYR	MY	CFY
ThI	97	17	1	0	0
FYS	3	54	15	0	0
FYR	0	29	83	1	16
MY	0	0	1	51	35
CFY	0	0	0	48	49

(b)

Ice Type	ThI	FYS	FYR	MY	CFY
ThI	83	26	2	0	0
FYS	14	49	11	0	0
FYR	3	25	86	1	11
MY	0	0	1	84	44
CFY	0	0	0	15	45

(c)

Ice Type	ThI	FYS	FYR	MY	CFY
ThI	96	4	0	0	0
FYS	4	76	13	0	0
FYR	0	20	86	1	10
MY	0	0	1	81	45
CFY	0	0	0	18	45

(d)

Ice Type	ThI	FYS	FYR	MY	CFY
ThI	98	5	0	0	0
FYS	2	70	15	0	0
FYR	0	25	84	1	12
MY	0	0	1	77	40
CFY	0	0	0	22	48

(e)

Ice Type	ThI	FYS	FYR	MY	CFY
ThI	98	6	0	0	0
FYS	2	74	12	0	0
FYR	0	20	87	1	9
MY	0	0	1	81	44
CFY	0	0	0	18	47

(f)

Ice Type	ThI	FYS	FYR	MY	CFY
ThI	98	13	0	0	0
FYS	2	83	8	1	0
FYR	0	3	65	31	31
MY	0	1	21	68	4
CFY	0	0	6	0	64

(g)

Ice Type	ThI	FYS	FYR	MY	CFY
ThI	96	12	0	0	0
FYS	4	86	6	0	0
FYR	0	1	87	7	34
MY	0	1	3	93	1
CFY	0	0	4	0	65

(h)

Ice Type	ThI	FYS	FYR	MY	CFY
ThI	95	13	0	0	0
FYS	5	84	5	1	0
FYR	0	1	87	11	32
MY	0	2	5	88	0
CFY	0	0	3	0	68

(i)

Ice Type	ThI	FYS	FYR	MY	CFY
ThI	95	42	1	0	0
FYS	5	47	17	6	0
FYR	0	8	59	5	30
MY	0	3	3	89	10
CFY	0	0	20	0	60

(j)

Ice Type	ThI	FYS	FYR	My	CFY
ThI	69	27	4	0	1
FYS	11	35	14	2	1
FYR	17	33	66	13	40
MY	1	3	2	82	17
CFY	2	2	14	3	41

(k)

Ice Type	ThI	FYS	FYR	MY	CFY
ThI	99	11	0	0	0
FYS	1	84	7	0	0
FYR	0	5	91	1	12
MY	0	0	1	98	10
CFY	0	0	1	1	78

(l)

Ice Type	ThI	FYS	FYR	MY	CFY
ThI	98	5	0	0	0
FYS	2	86	8	0	0
FYR	0	9	90	1	13
MY	0	0	1	98	2
CFY	0	0	4	1	75

TABLE 5. Table of ice fractions (%) at various polarizations and frequencies. Columns without any polarization denoted indicate that the complete polarimetry is used. An asterisk indicates errors are present due to the contribution of a significant number of misclassified pixels to the totals shown.

Ice Fraction	C_{HH}	C_{VV}	C	L_{HH}	L_{VV}	L	L_{HH}, C_{VV}	L_{HH}, C_{HH}	L, C
Old (MY)	40*	40*	40*	40*	40*	25	27	26	25
Thick (MY,CFY)	40	40	40	40	43	38	41	41	42
Thin (ThI)	3	5	3	4	5	4	4	4	3

LIST OF FIGURES

Figure 1. SAR amplitude image of sea-ice in the Beaufort Sea, Alaska, acquired by AIRSAR at a center location of $73^{\circ}2.9'N, 142^{\circ}17.1'W$ at 17:19:55 GMT on March 11, 1988 (Image 1372) at (a) C-band frequency, VV-polarization (top left); and (b) L-band frequency, HH-polarization (bottom left); (c) MAP classification of L- and C-band fully polarimetric SAR data into 6 ice types (top right); (d) Brightness temperature T_B from NORDA Ka-band radiometer microwave system (bottom right).

Figure 2. SAR amplitude image of sea-ice in the Beaufort Sea, Alaska, acquired by AIRSAR at a center location of $72^{\circ}38.2'N, 143^{\circ}48.1'W$ at 04:35:08 GMT on March 19, 1988 (Image 311) at (a) C-band frequency, VV-polarization (top left); and (b) L-band frequency, HH-polarization (bottom left); (c) MAP classification of L- and C-band fully polarimetric SAR data into five ice types (no ThI) (top right). The APLIS'88 ice camp (bright return) is located at the edge of a multi year ice floe (darker background).

Figure 3. Daily observations of air-temperatures, atmospheric pressure, and wind direction and speed collected at APLIS'88 between March and April, from Wen and others (1989).

Figure 4. Air photo of the APLIS88 ice camp looking North, showing areas of compressed first-year ice (CFY), multi year ice (MY), deformed first-year ice (FYRR), and first-year smooth (FYS).

Figure 5. Air photo of the APLIS88 ice camp looking South.

Figure 6. Ice characteristics of an ice core taken from the FY ice lead near the Ice Camp APLIS'88 on March 25, 1988, from Wen and others (1989).

Figure 7. Radar backscatter curves σ of 6 ice types identified in Image 1372 versus the incidence angle θ_i at (a) C-band HH-polarization; (b) C-band HV-polarization; (c) L-band HH-polarization; (d) L-band HV-polarization. Vertical lines indicate the limits of the 3 regions used for clustering of the multi-parameter SAR data.

Figure 8. Histogram of the real part of the dielectric constant of thin ice in Image 1372 at L-band frequency using the small perturbation model. The median value of the distribution is $\epsilon_r = 6$, and the standard deviation is 4.5.

Figure 9. Classification map of Image 1372 into 6 sea-ice types at (a) C-band VV-polarization; (b) L-band HH-polarization; (c) C-band VV-polarization and L-band HH-polarization combined; (d) L-band polarimetric.

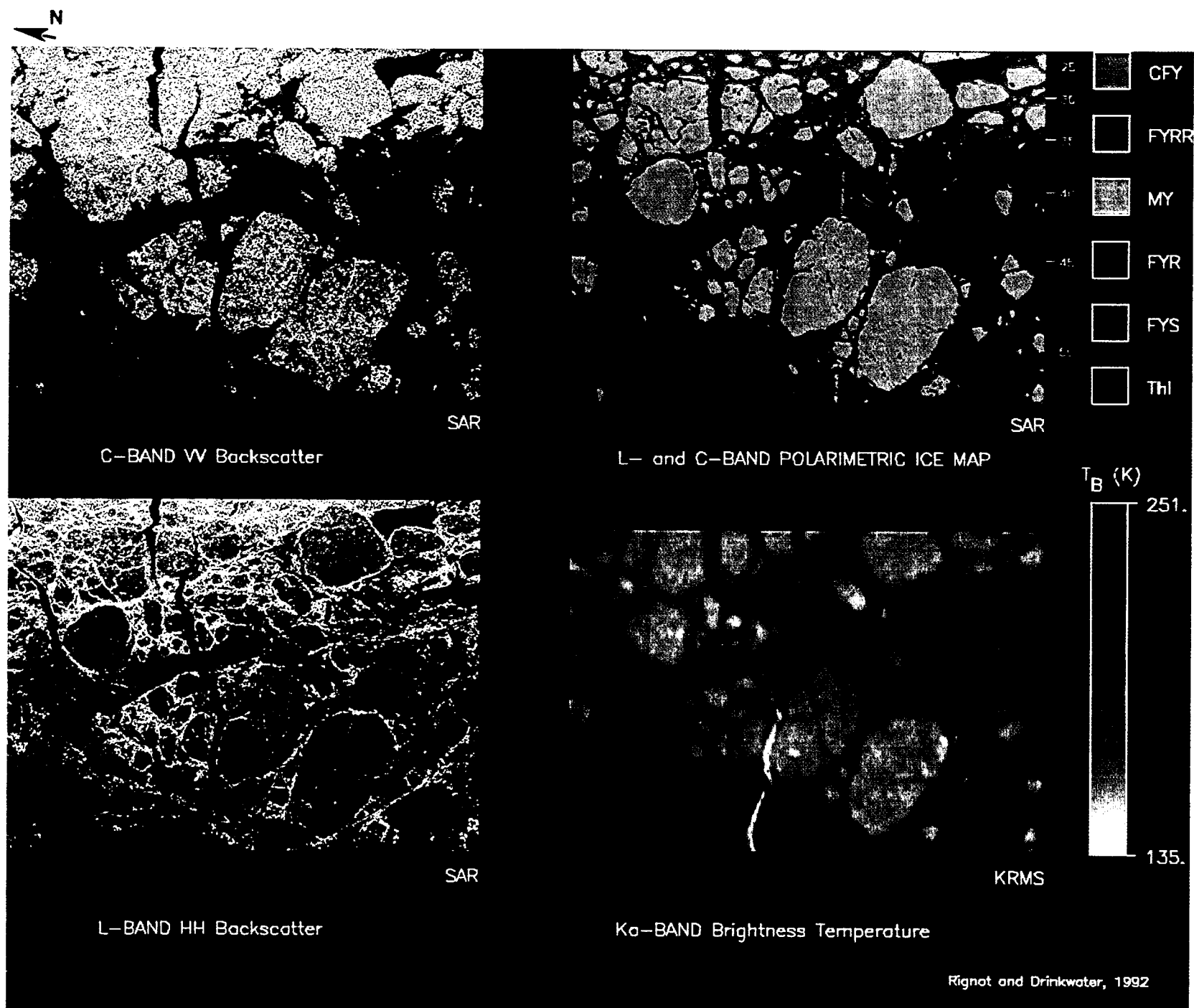


FIGURE 1.

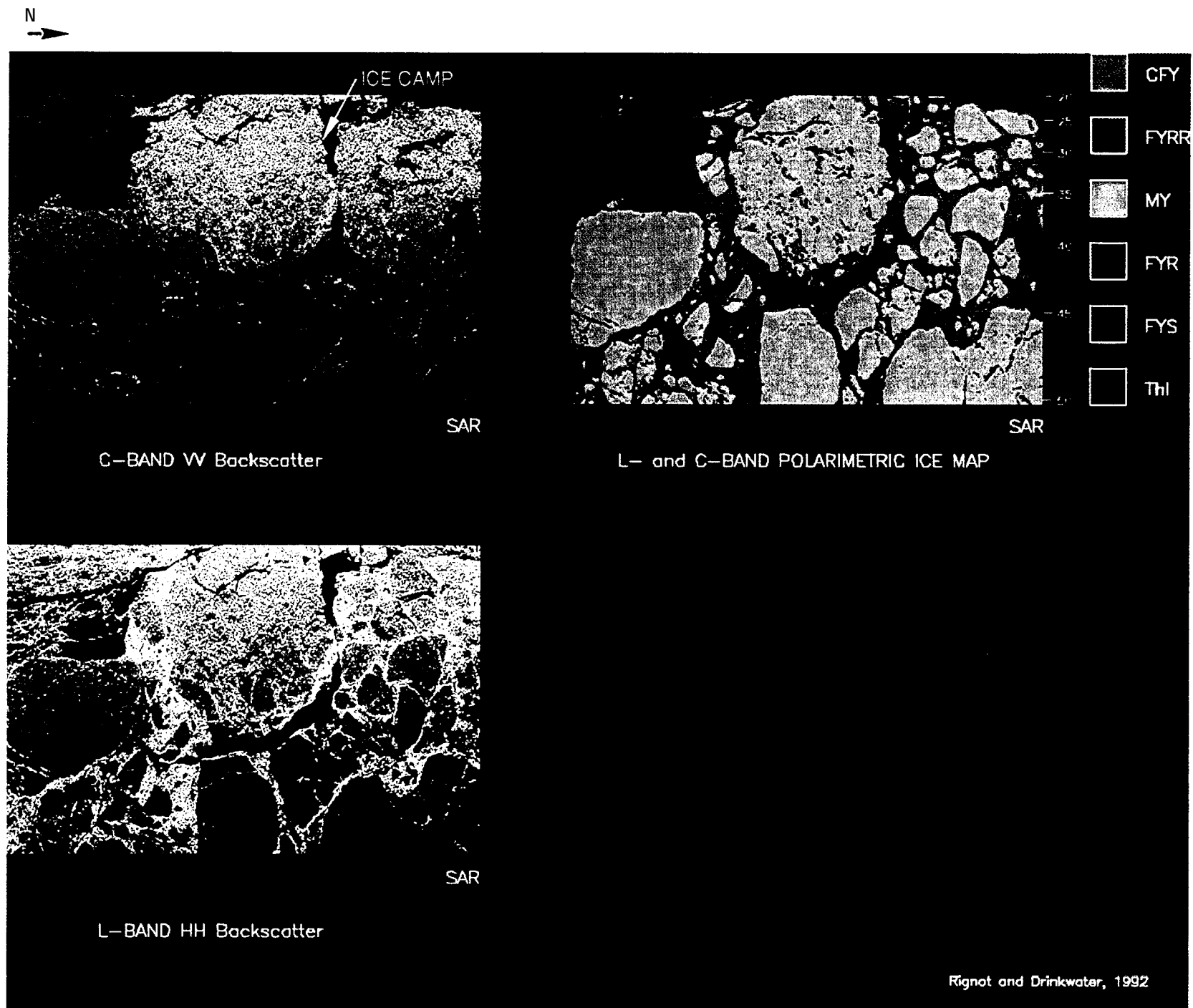


FIGURE 2.

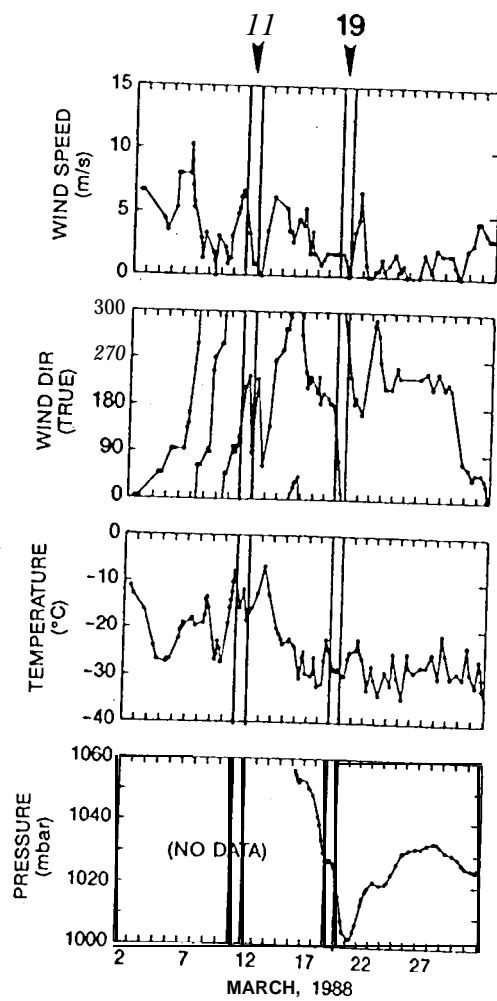


FIGURE 3.

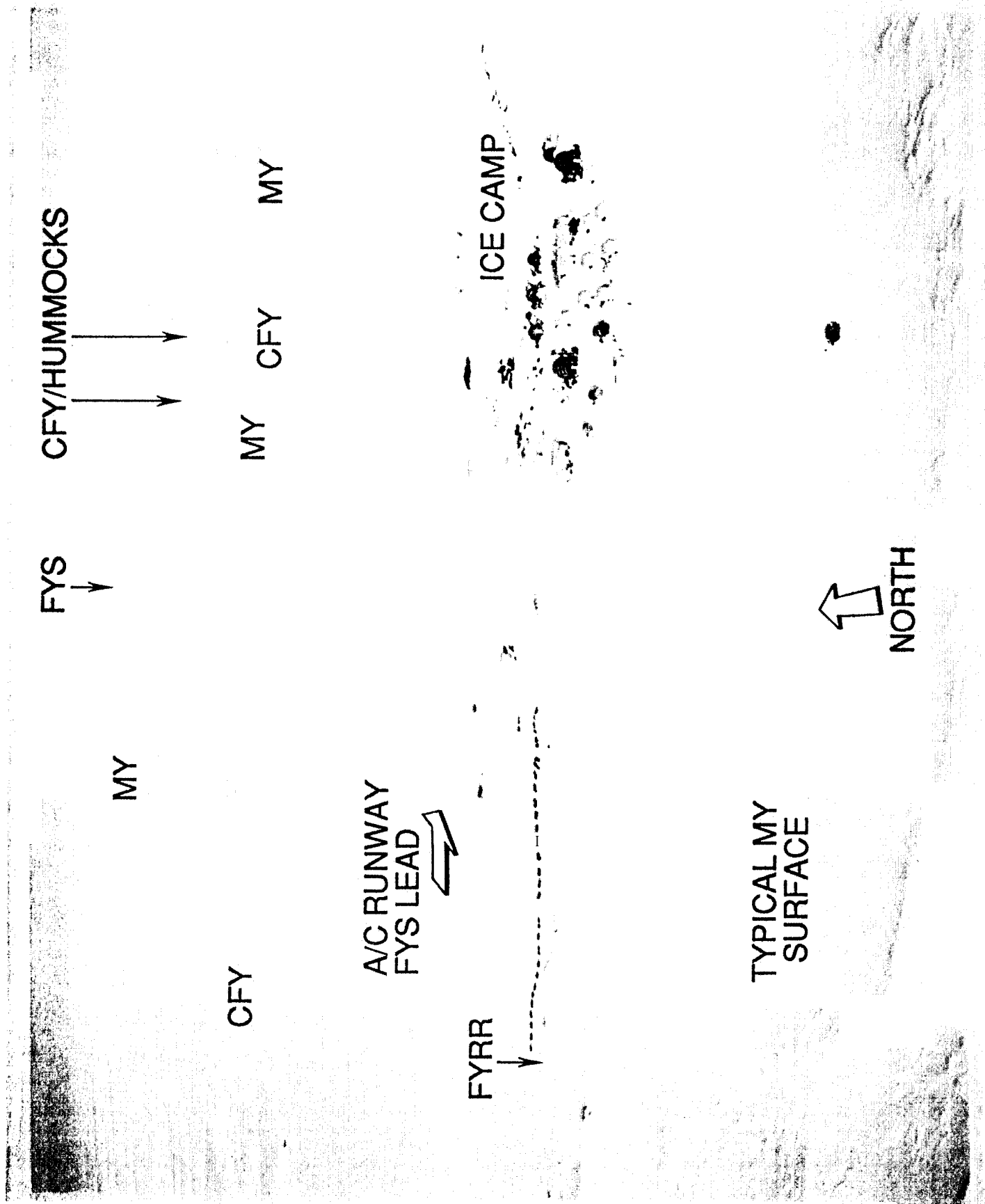


FIGURE 4.

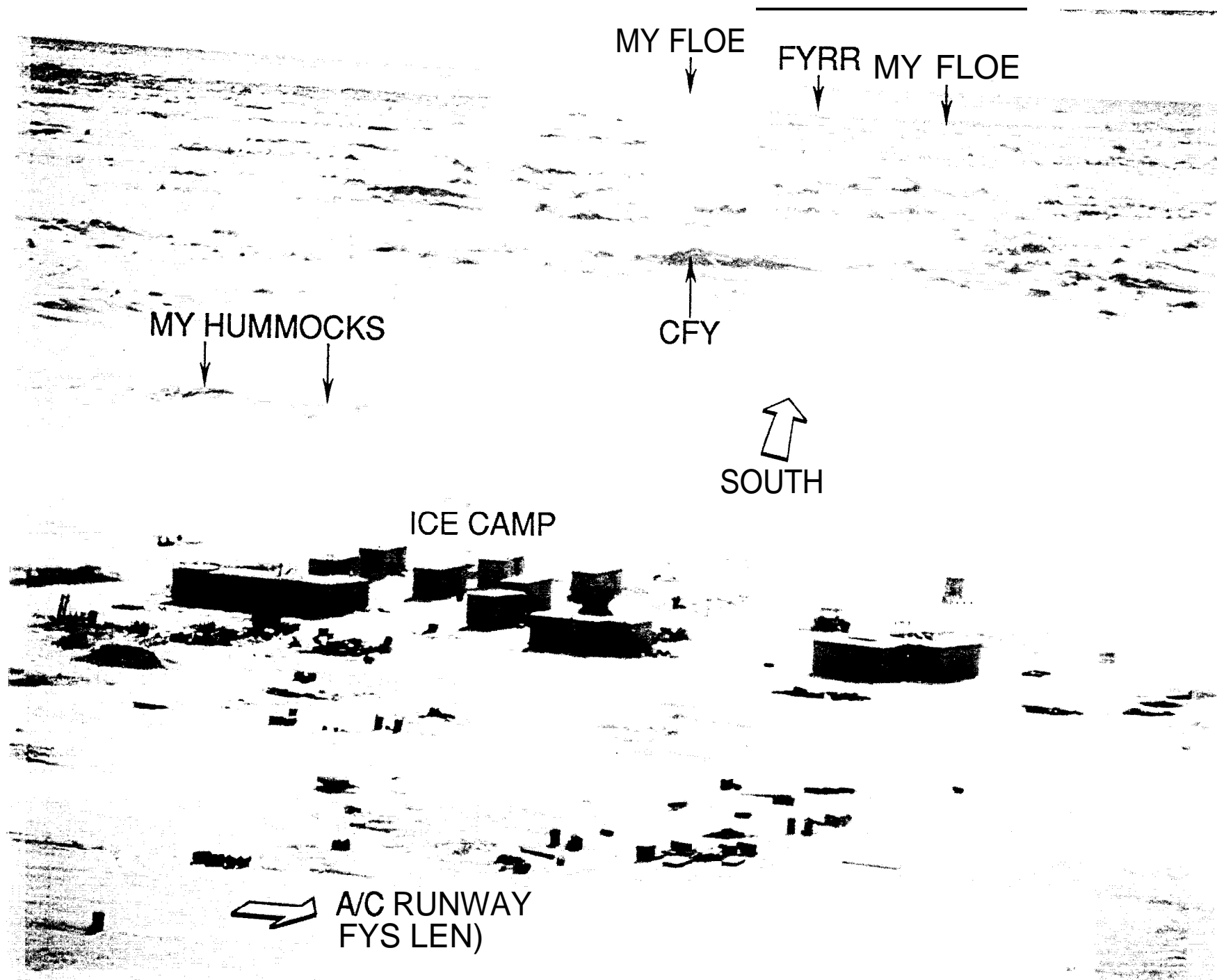


FIGURE 5.

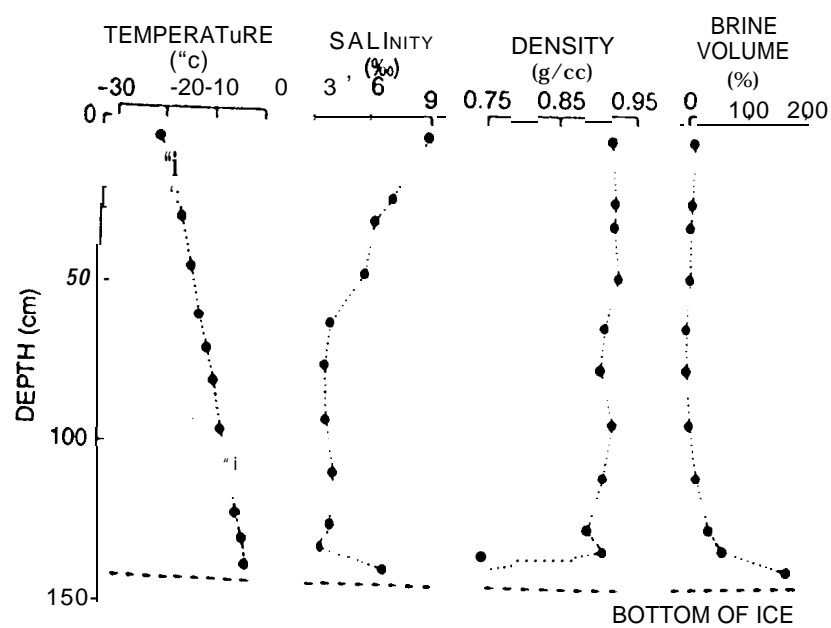


FIGURE 6.

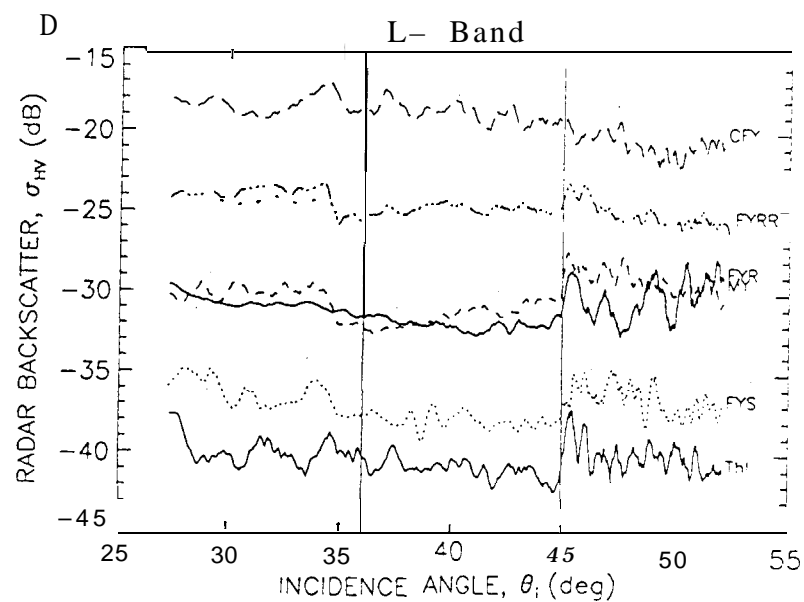
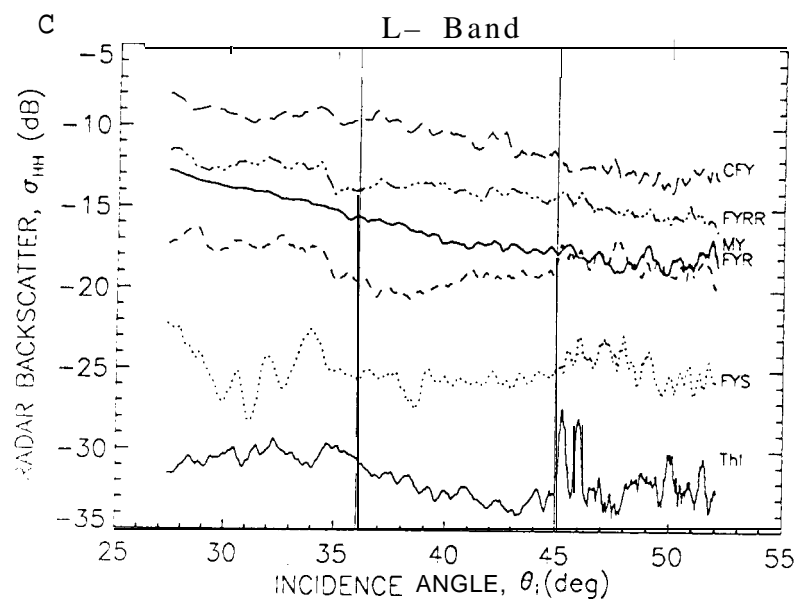
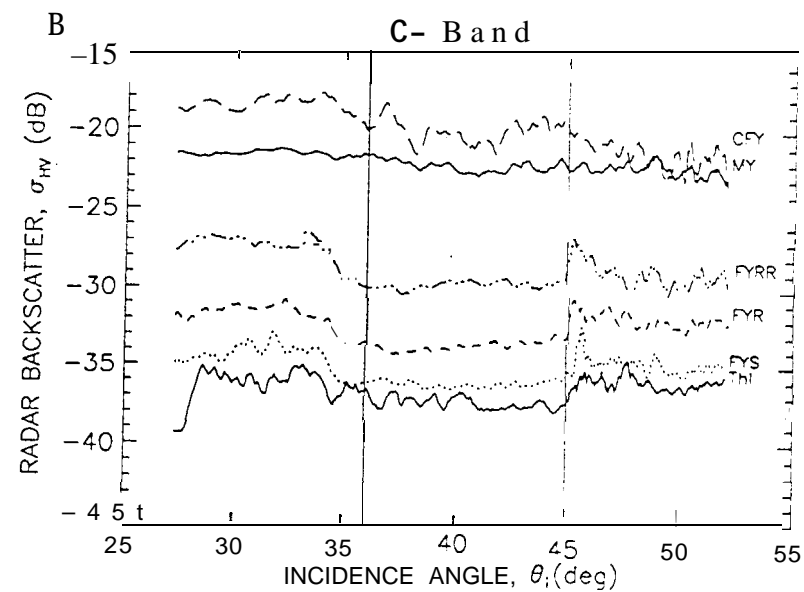
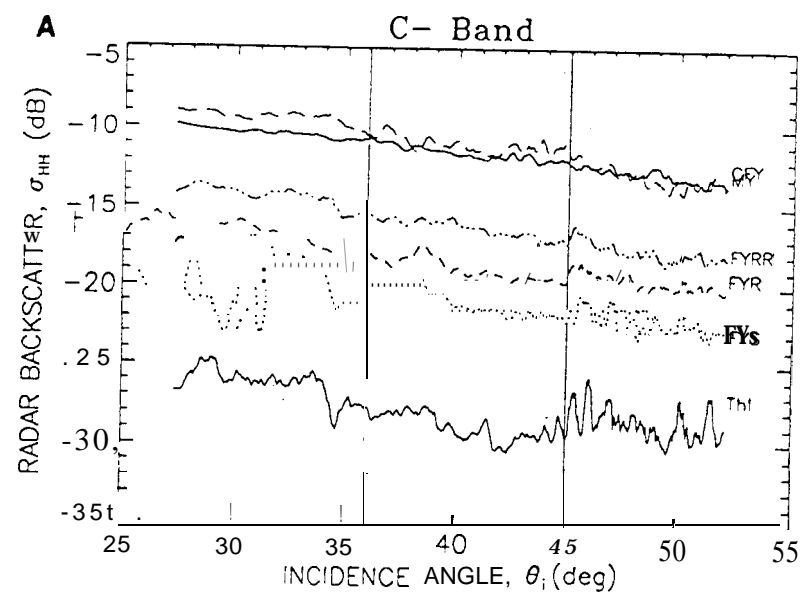


FIGURE 7.

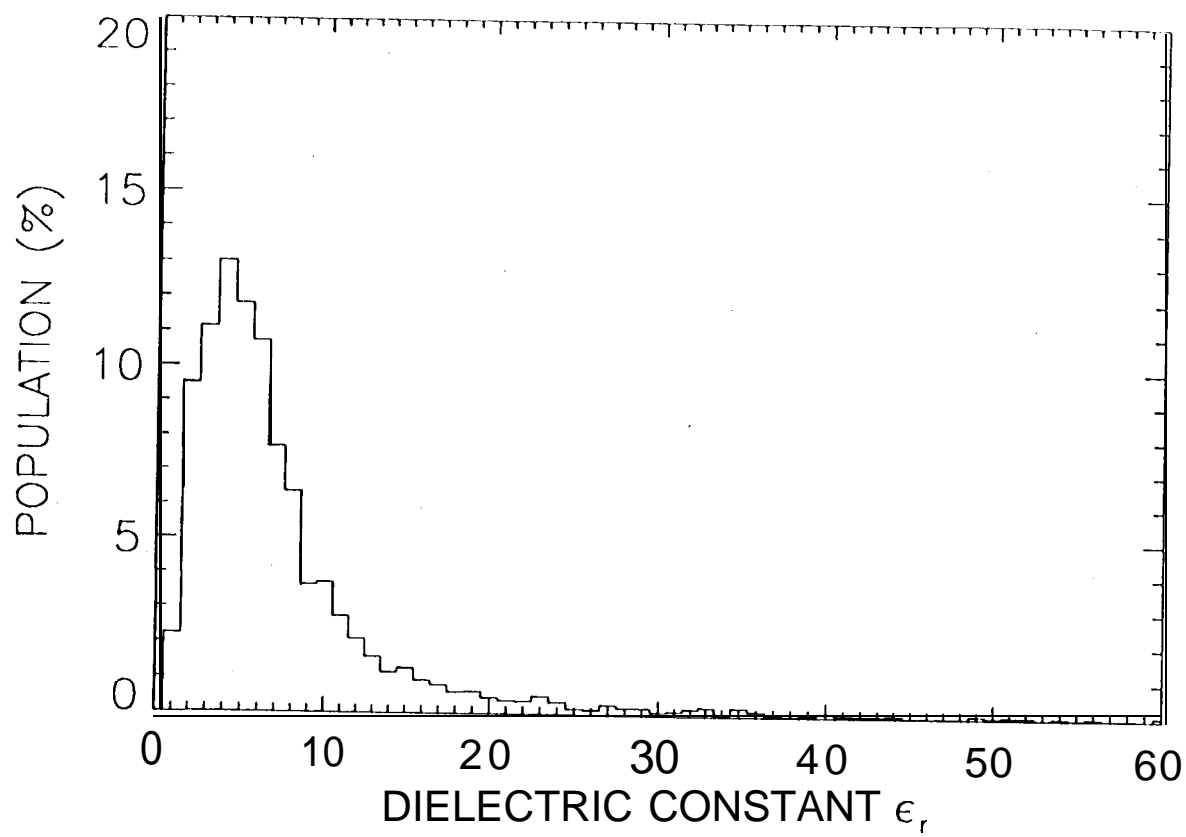
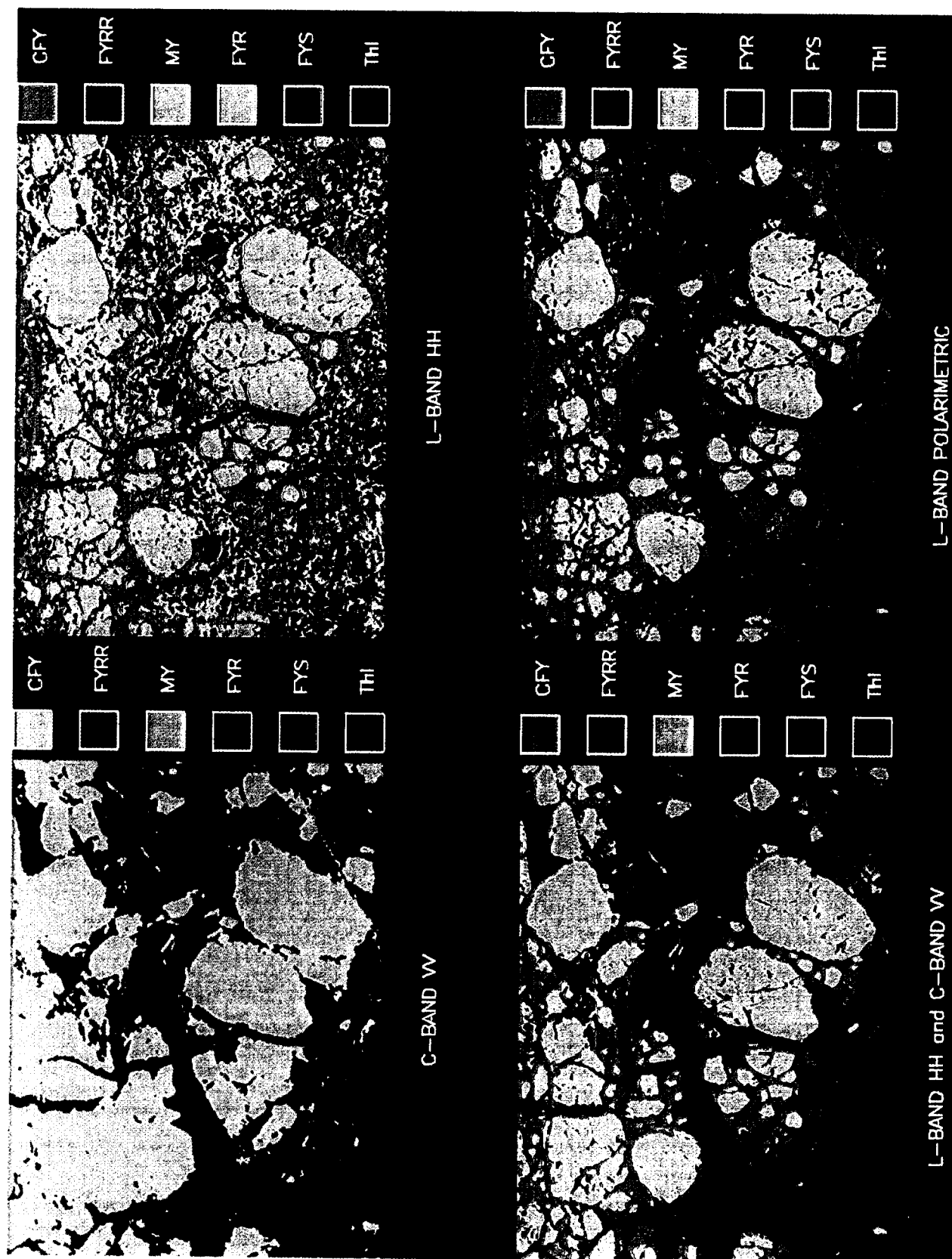


FIGURE 8.



Rignot and Drinkwater, 1992

FIGURE 8.